Journal of Materials Chemistry A

PAPER

View Article Online
View Journal | View Issue

Check for updates

Cite this: J. Mater. Chem. A, 2019, 7, 6543

In situ synthesized low-PtCo@porous carbon catalyst for highly efficient hydrogen evolution†

Yudao Qin,[a] Xiaoyu Han,[a] Srinivas Gadipelli,[a] Jian Guo,[a] Shijie Wu,[b] Liqun Kang,[c] June Callison[ad] and Zhengxiao Guo *[ae]

Received 19th December 2018
Accepted 5th February 2019

DOI: 10.1039/c8ta12263f

rsc.li/materials-a

Electrochemical water splitting is a sustainable method for producing hydrogen—the ultimate clean energy carrier. However, high cost and poor stability of the Pt catalyst for hydrogen evolution reaction (HER) hinder its wide applications. Here, we report a facile approach to synthesize an ultra-low PtCo bimetallic catalyst embedded in porous carbon *via* direct annealing of Pt-doped ZIF-67. The resulting catalyst (CPt@ZIF-67) with only 5 wt% Pt loading exhibits better performance than commercial 20 wt% Pt/C, achieving a Tafel slope of 27.1 mV dec^{-1} with an overpotential of only 50 mV at current density of 10 mA cm^{-2}. Theoretical simulations show that carbon cages generated over the bimetal clusters during annealing dramatically reduce the free energy for HER. The free energy does not reduce proportionally with increasing Pt loading, implying the need to ensure appropriate Pt placement on surfaces, rather than simply raising Pt level, in order to enhance effectiveness of a Pt-based catalyst. The study provides a viable approach for developing cost-effective Pt-related catalysts for HER.

Open Access Article. Published on 25 February 2019. Downloaded on 2/7/2026 11:01:58 AM.
This article is licensed under a Creative Commons Attribution 3.0 Unported Licence.

Introduction

Clean and sustainable energy sources are highly desirable for both reduction of carbon dioxide emission and reliance on pollutive fossil fuels. Hydrogen is an ideal choice due to its elemental abundance, high energy density per unit mass (143 kJ g^{-1}) and zero carbon emission at point of use.[1,2] Industrial hydrogen is manufactured by steam methane reforming and coal gasification, in which CO_2 emission persists unless effective CO_2 capture is implemented. In contrast, electrocatalytic water-splitting, using off-peak electricity, offers a cost-effective path to produce hydrogen (Table S1†).[3] Commercial Vulcan XC72 platinum on carbon (20 wt% Pt/C) is the benchmark catalyst for the hydrogen evolution reaction (HER), as it requires a very small overpotential. However, the noble-metal catalyst is costly and prone to detachment from the carbon support during cycling. Thus, it is desirable to develop low-cost, highly efficient and stable alternatives for HER.[4–6]

One straightforward strategy is to lower the Pt loading but preserve its performance. Several approaches have been proposed in the past, one of which is to dope Pt into fine structures to maximise Pt exposure or active sites.[7–9] Tang *et al.* studied platinum nanowires grown on single-layered nickel hydroxide, Pt NWs/SL-Ni(OH)$_2$, and showed HER performance comparable with commercial 20 wt% Pt/C.[7] However, the synthesis method is arduous and time-consuming. Another approach is to adopt alternative transition metals to Pt. A nanocrystalline Ni_5P_4 and its related phosphorous compounds have been reported to exhibit good HER performance.[10] However, they utilize hydrogen in the annealing procedure, which conflicts with the initial purpose of hydrogen production from water. Recently, nitrogen-doped graphene with a small amount of transition metal clusters[11–13] has also exhibited HER activity, as nitrogen can induce active sites, but the HER activity is much lower than that of 20 wt% Pt/C, as the Tafel slope is more than 2.6 times larger than its commercial counterpart.[13]

Inspired by the above studies, zeolitic imidazolate framework (ZIF-67) (Co-2-methylimidazole) was selected as the precursor for a nitrogen doped carbon skeleton,[14,15] as well as a transition metal provider for anchoring Pt to minimize metal clustering *via* direct annealing under N_2 atmosphere (Scheme 1).[16–19] The resulting encapsulated-Pt and nitrogen-doped carbon framework catalysts demonstrated excellent HER activity and long-term stability, outperforming the commercial counterpart, particularly at low potential in an acidic electrolyte, as ZIF-67 provided a skeletal structure for Pt to form an alloy and prevent clustering during the annealing process. Moreover, Hubbard-corrected density functional theory (DFT+U)

[a]Department of Chemistry, University College London, 20 Gordon Street, London, WC1H 0AJ, UK. E-mail: z.x.guo@ucl.ac.uk; Tel: +44 (0)20 7679 7527

[b]Semiconductor Measurement Solutions, Keysight Technologies, Inc., Santa Clara, California 95051, USA

[c]Department of Chemical Engineering, University College London, Torrington Place, London, WC1E 7JE, UK

[d]UK Catalysis Hub, Research Complex at Harwell (RCaH), Rutherford Appleton Laboratory, Harwell Oxon, OX11 0FA, UK

[e]Departments of Chemistry and Mechanical Engineering, Zhejiang Institute of Research and Innovation, University of Hong Kong, Hong Kong SAR

† Electronic supplementary information (ESI) available. See DOI: 10.1039/c8ta12263f

Open Access Article. Published on 25 February 2019. Downloaded on 2/7/2026 11:01:58 AM.
This article is licensed under a Creative Commons Attribution 3.0 Unported Licence.

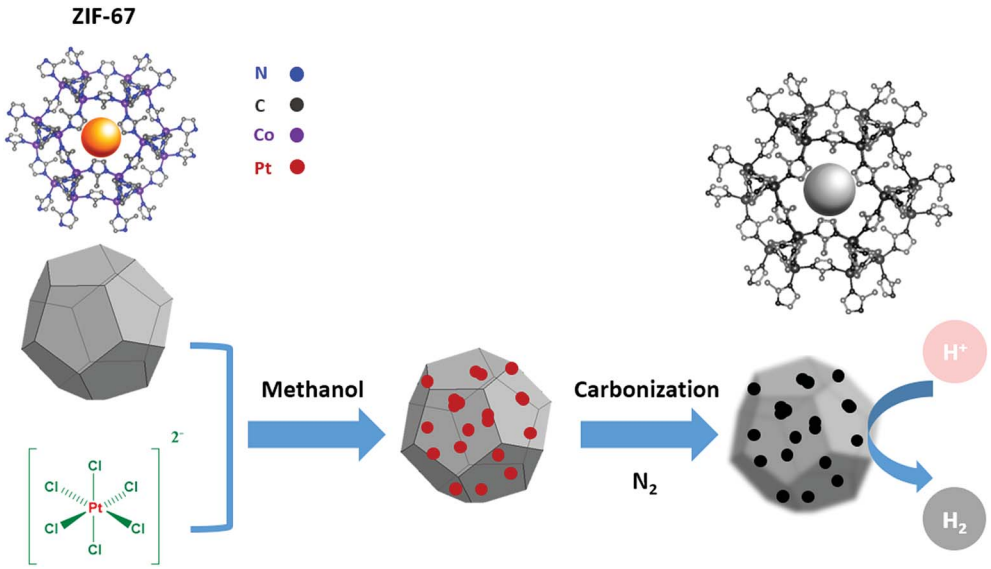

Scheme 1 Illustration of the synthesis procedures of carbon-encapsulated Pt-doped alloy embedded in nitrogen-doped carbon framework.

simulations revealed that the free energy of the HER reaction could be dramatically tuned by use of different ratios of the metal alloy inside the carbon cage. The Pt atom tended to dope at the edge positions of the Co clusters at a low concentration, but inhabited bulk positions with increasing Pt loading, indicating that not all Pt atoms will act as active sites in the alloy clusters. Hence, HER performance does not increase proportionately with Pt content in the system and dilute Pt doping can be very cost-effective in future catalyst designs for HER. Our results provide not only a strategy of efficient utilization of noble metal elements in HER, but also a practical route for low-cost synthesis of such alloy catalysts. The simple synthesis procedure also offers strong potential for industrial scale-up.

Experiments

All chemicals were purchased from Sigma-Aldrich and used without any purification unless otherwise noted.

Synthesis ZIF-67

First, cobalt nitrate hexahydrate (7.185 g) was dissolved in 500 mL methanol. Then, 2-methylimidazole (8.106 g) was dissolved in another 500 mL methanol. The latter solution was slowly added to the former in a 1 L wide mouth jar while stirring at room temperature. Stirring proceeded for 2 h, after which the solution was left to settle for 24 h. The clear top solution was drained and the purple precipitates were collected by centrifugation with further methanol washing. The samples were dried in an oven at 80 °C for 24 h.

Synthesis of Pt@ZIF-67 and CPt@ZIF-67

As-synthesized ZIF-67 crystal powder (100 mg) and chloroplatinic acid hexahydrate $H_2PtCl_6 \cdot 6H_2O$ (26 mg) were added into methanol (20 mL). Sonication and stirring were carried out for 1 h to achieve a homogenous inky solution. Pt-coated ZIF-67 (Pt@ZIF-67) was obtained by grinding the purple solid into fine powder after evaporating the methanol in the oven at 80 °C for 24 hours. Then, the product was carbonized at 900 °C (heating rate of 5 °C min^{-1}) in an alumina boat (1 × 1.5 × 5 cm) in a horizontal tube furnace to form carbonized ZIF-67 with Pt doping, termed CPt@ZIF-67. The powders were annealed at 900 °C for 6 hours under nitrogen and cooled to room temperature. After carbonization, black solids were collected and ground into fine powder. To optimize the carbonization procedure, sample synthesis was carried out at different temperatures and durations, termed CPt@ZIF-67-*x* °C-*y* h, where *x* and *y* represent the temperature and duration of the carbonization.

Characterizations

Powder X-ray diffraction (PXRD, Stoe Stadi-P, Cu-K-alpha and Mo-K-alpha) was carried out by encapsulation of samples in a 0.5 mm diameter borosilicate glass capillary under ambient conditions. X-ray photoemission spectroscopy (XPS, Al-K-alpha, Thermo Scientific) and scanning electron microscopy (SEM, Jeol) were carried out on carbon tape. Transmission electron microscopy (TEM, Jeol) measurements were completed on a carbon-coated copper TEM grid support. Raman spectroscopy (514.5 nm laser, Renishaw) was carried out with powder samples on a glass slide. Atomic force microscopy measurements were carried out in AC mode using silicon rectangular-shaped cantilevers with a tip curvature radius of 6 nm and a force constant of 40 N m^{-1}. The test samples were prepared by dip-coating the materials on clean silicon substrate. (AFM, Keysight 5600LS). The Pt content was measured by microwave plasma atomic emission spectroscopy (Agilent 4210 MP-AES).

Electrochemical tests

All tests were carried out using an Autolab (Metrohm PGSTAT302N) electrochemical station, using a three-electrode

 This journal is © The Royal Society of Chemistry 2019

Open Access Article. Published on 25 February 2019. Downloaded on 2/7/2026 11:01:58 AM.
This article is licensed under a Creative Commons Attribution 3.0 Unported Licence.

method with a glassy carbon rotating disk as the working electrode and carbon rod and Ag/AgCl/saturated KCl as counter and reference electrode, respectively, in an acidic electrolyte (0.5 M H_2SO_4) at room temperature. All measurements were carried out with a fixed catalyst deposition of ~0.26 mg cm^{-2} on a 3 mm diameter (area of 0.0707 cm^2) glassy carbon disk electrode. The catalyst was prepared as follows: 2 mg of sample was dispersed in a 540 μL solution consisting 500 μL of 4 : 1 v/v water/ethanol and 40 μL of Nafion (5% solution) under sonication. The sonication was carried out up to an hour to get uniform dispersion of catalyst ink, of which 5 μL was micropipetted and dropped on a glassy carbon disk electrode followed by drying at 60 °C in the oven. All electrochemical test results are reported with respect to the reference Ag/AgCl. The linear sweep voltammetry (LSV) curves were recorded with voltage sweeping at 10 mV s^{-1} in the potential range of +0.0 V to −0.7 V with disk rotating speed of 1600 rpm in 0.5 M H_2SO_4. The data were collected after stable CVs were obtained. The measured potentials against Ag/AgCl were converted to RHE using the following relation: in 0.5 M H_2SO_4, $E_{(RHE)} = E_{Ag/AgCl} + 0.059\ pH + E^{o}_{Ag/AgCl}$, where $E^{o}_{Ag/AgCl} = 0.1976$ V at 25 °C and $E_{Ag/AgCl}$ is the working potential. The overpotential $E = E_{(RHE)} - 1.23$ V.

Density functional theory (DFT) simulations

All calculations were carried out based on density functional theory, in the Vienna ab initio package (VASP).[20,21] The Perdew–Burke–Ernzerhof (PBE) functional[22] was used for the exchange–correlation term with the projector augmented wave method.[23,24] A plane wave cutoff of 500 eV with forces converged to 0.01 eV $Å^{-1}$ was employed. Considering the cobalt carbon interaction, on-site Hubbard U corrections (3.3) were selected for the Co delocalized d electrons, as has been assessed in the past.[25,26] Spin polarization was counted in all calculations. Gamma only was selected for the K-point sampling.

The free energies of the intermediates were obtained by

$$\Delta G(\mathrm{H}^*) = \Delta E(\mathrm{H}^*) + \Delta ZPE - T\Delta S$$

where $\Delta E(\mathrm{H}^*)$ is the adsorption energy calculated by

$$\Delta E(H^*) = E_{\mathrm{H@core-shell}} - E_{\mathrm{core-shell}} - \frac{1}{2}E_{\mathrm{H_2}}$$

ΔZPE is the zero-point energy change, and ΔS is the entropy change of adsorption H. All analysis within DFT scope used normal-mode analysis, as proposed by Nørskov.[27]

$$\Delta ZPE(\mathrm{H}^*) = ZPE(\mathrm{H}^*) - \frac{1}{2}ZPE(\mathrm{H_2})$$

where $ZPE(H_2)$ is 0.27 eV.[28] Since the vibration frequency of H is less than 1 meV, $\Delta S = S(\mathrm{H}^*) - 0.5 \times S(\mathrm{H_2}) \approx -0.5S(\mathrm{H_2})$. For H_2 at 300 K and 1 atm, $TS(H_2) = 0.41$ eV. Then $T\Delta S \approx -0.2$ eV.

Results and discussion

Carbon-encapsulated Pt-alloy carbon network, hereafter referred to as CPt@ZIF-67, was synthesized by a two-step approach, modified from previous work of Gadipelli *et al.*[19] First, ZIF precursors and platinum salt were completely dissolved in methanol by sonication and stirring; then, the solvent was evaporated and the as-synthesized material was annealed in an inert N_2 atmosphere at a given temperature to yield the final sample. For comparison, carbonized ZIF without the Pt salt was also prepared, denoted CZIF-67. The procedures are illustrated in Scheme 1 and were detailed in the Experiments section.

First, carbonization temperature and duration were optimized from 600 to 1000 °C for 2 or 6 hours. These samples were denoted as CPt@ZIF-67-*x*-*y*, where the carbonization process is at x °C for y hours. The morphology of the pre-annealing samples was studied by AFM and SEM. Before annealing, the samples show clear polyhedral structures (Fig. S2a, b, S3b and S4a†). The AFM height profile measurements (Fig. S2c†) indicate that the particle sizes of Pt@ZIF-67 vary from 0.8 to 1.5 μm. After annealing, the samples became amorphous (Fig. S4†). The degree of amorphization gradually increased with the increasing carbonization temperature and duration, which is in line with previous observations.[29] For CPt@ZIF-67-600-2 (Fig. S4b†) and CPt@ZIF-67-700-2 (Fig. S4c†), the crystalline cubic ZIF morphology became spherical on the edges. When the annealing temperature increased to 900 °C and above, the original structure fully collapsed into an amorphous structure (Fig. S4f–h†). Hence, the optimum carbonization temperature and duration are 900 °C and 6 hours. The optimized CPt@ZIF-67-900-6 also showed effective catalysis performance, with the lowest onset potential and the highest current density compared with those from other carbonization conditions, as will be illustrated later. Hence, all the samples used were 900 °C-6 h, unless specified otherwise.

TEM images (Fig. 1a–c) show that the size of the PtCo alloy clusters in CPt@ZIF-67 is 2.7 nm on average, almost half the particle size (5.2 nm on average) of the commercial 20 wt% Pt/C (Fig. S6e†). Meanwhile, the densities of the metal clusters in CPt@ZIF-67 and 20 wt% Pt/C were at a comparable level (Fig. 1b and S6d† or Fig. S6a and S6e†). Hence, the metal particles of our samples are one eighth scale of the commercial ones.

By tailoring the carbonization conditions, the graphitic or graphene shell may still be structurally porous or of variable thickness, *i.e.* not completely covering the whole cluster or with only one or two graphene layers, allowing easy access of electrolyte to the catalytic metal sites while protecting the clusters from further growth and aggregation.[30,31] As a result, the catalyst is expected to be effective and stable over a long period of service.

The high crystallinity of the PtCo alloy is shown in Fig. 1a, with a lattice spacing of 0.23 nm corresponding to the PtCo(111) plane.[32] Elemental mapping (Fig. 1e–h) reveals that both Pt and Co elements distribute homogenously in the alloy. Meanwhile, the elemental mapping of Pt@ZIF-67 (Fig. S7†) indicates that these elements are uniformly distributed even before annealing.

Further, structural analysis was carried out using PXRD patterns. Before annealing (Fig. S8a†) the peaks of samples with and without Pt doping appeared at the same positions in strong contrast with the baseline. This indicates the high crystallinity

Open Access Article. Published on 25 February 2019. Downloaded on 2/7/2026 11:01:58 AM.
This article is licensed under a Creative Commons Attribution 3.0 Unported Licence.

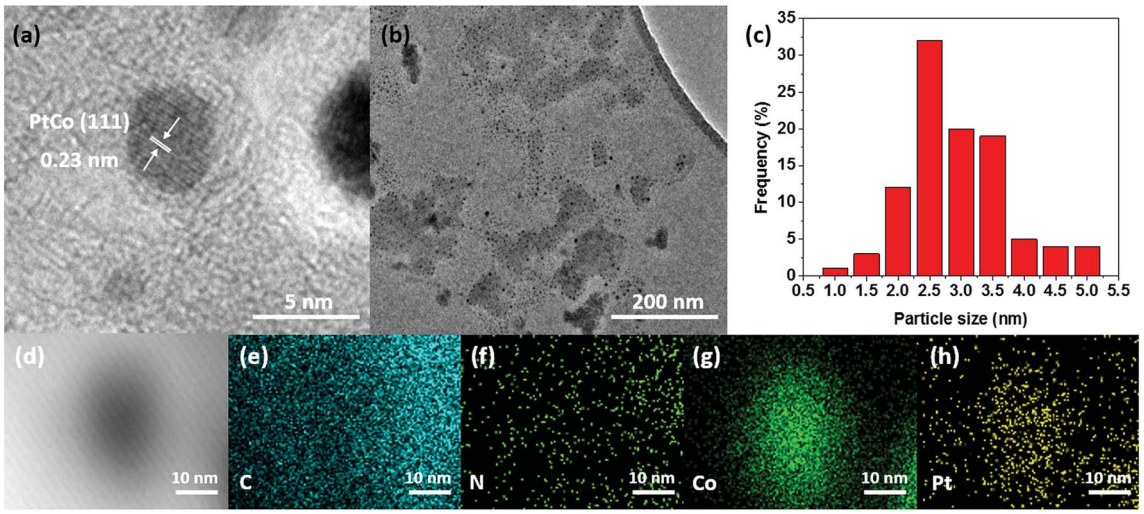

Fig. 1 (a) Lattice spacing of PtCo alloy clusters in CPt@ZIF-67. (b) TEM image of CPt@ZIF-67. (c) The size distribution of clusters in CPt@ZIF-67, from the diameters of 100 randomly selected nanoparticles (average diameter = 2.7 nm). (d) TEM image of CPt@ZIF-67. Element mappings of (e) carbon, (f) nitrogen, (g) cobalt, and (h) platinum.

of the pre-annealed samples and that Pt was well distributed without disturbing the ZIF structure.[33,34] After annealing, peaks at 44.2° and 51.3° of CZIF-67 could be assigned to Co (111) and (200) (JCPDS 15-0806) (Fig. S8c†).[35] Blue shifts of those peaks were observed in the CPt@ZIF-67 sample, due to the Pt atoms alloyed in the Co cluster structure leading to lattice expansion.[32,36] Meanwhile, the closeness of peaks when compared to those of CZIF-67 indicates that a limited amount of Pt atoms is alloyed into the Co lattice. The Mo-radiation PXRD of CPt@ZIF-67 is shown in Fig. S8e;† the peaks can be indexed as C (002),[19] Co_3O_4 (311),[37] PtCo (111)[38] and PtCo (200),[32] which indicates that the catalyst consists of carbon, cobalt oxide and platinum cobalt alloys.

Raman spectroscopy measurements were carried out and are shown in Fig. S9.† The D band peak (signature disorder-induced sp^2-hybridized graphitic carbon often activated by defects) and the G band peak (the ordered graphitic carbon with stretching vibrations) are located at 1340 and 1596 cm^{-1}, respectively. Moreover, the high I_D/I_G ratio of CPt@ZIF-67 indicated that the carbonized ZIFs possessed graphitic characteristics with abundant defect concentration (Fig. S9a†).[39] Another relatively weak 2D broad peak located at 2652 cm^{-1} indicates that the metal core contact doped electrons to the carbon cages.

The surface composition and chemical and electronic states of CPt@ZIF-67 were characterised by XPS. As shown in Fig. S10a,† comparison of CPt@ZIF-67 and CZIF-67 proved the formation of Pt alloy. In Fig. 2a, three distinct peaks at 398.4, 400.6 and 402.3 eV can be assigned to pyridinic N, graphitic N and quaternary N, respectively.[40,41] The formation of pyridinic N in the annealed sample indicates that the carbonization led to more stable six-membered rings (Table S2†). The Co and Pt spectra of CPt@ZIF-67 are shown in Fig. 2b and c, respectively. The two peaks in each spectrum could be assigned to Co $2p_{3/2}$ and Co $2p_{1/2}$ and Pt $4f_{7/2}$ and Pt $4f_{5/2}$, respectively. Compared with the pure Pt metal peaks in 71.4 and 74.5 eV, notable shifts of Pt in CPt@ZIF-67 to 71.9 and 75.1 eV were observed.[42] This positive shift was due to the charge transfer from transition metal Co to noble metal Pt in the alloy, which is in line with our PXRD analysis.[43]

The Brunauer–Emmett–Teller (BET) surface area and pore size distribution were obtained by N_2 sorption isotherms. The calculated surface areas of CPt@ZIF-67, CZIF-67 and Pt@ZIF-67 were 90.1 $m^2\ g^{-1}$, 330.2 $m^2\ g^{-1}$ and 1516.2 $m^2\ g^{-1}$, respectively (Fig. S11a–c†). The pore size distributions were also investigated. As shown in Fig. S11d–f,† the CPt@ZIF-67 possessed larger pore size than CZIF-67 and Pt@ZIF-67, mainly concentrated in the range of 4 to 6 nm (Fig. S11d†). In contrast, the pore size ranges of CZIF-67 and Pt@ZIF-67 were focused within 1–4 nm and 1–2 nm, respectively. (Fig. S11e and f†). Hence, the CPt@ZIF-67, with mesoporous characteristics, effectively promotes electrolyte penetration and charge transfer, even while possessing much less surface area.

Both MP-AES and XPS were employed to determine the Pt loading and near-surface composition of the Pt in the alloy cluster, respectively. The MP-AES results show that the average Pt loading in the catalysts is ~5 wt%, which is comparable with the level of an atomic layer deposition (ALD) synthesis depositing single Pt atoms on nitrogen doped graphene.[4] To eliminate error, six points were selected from the XPS analysis to give a mean value of 0.93 wt% Pt in the near-surface region of the catalyst, as detailed in Table S3.† Collective results show that CPt@ZIF-67 is of much lower Pt content than the commercial 20 wt% Pt/C.

The electrocatalytic HER capability of the catalysts was studied using steady-state LSV on a glassy carbon disk electrode in 0.5 M H_2SO_4. The LSV curves of CPt@ZIF-67 are shown in Fig. 3a with those of CZIF-67, carbon black and 20 wt% Pt/C for comparison. Overall, the catalysts with Pt loading outperform those without. To achieve a reference current density of 10 mA cm^{-2}, the alloy CPt@ZIF-67 required a 50 mV overpotential, which was 5 mV lower than 20 wt% Pt/C (55 mV). Tafel slopes of the four samples are plotted in Fig. 3b. The values are 167.9, 27.1, 331.8 and 35.5 mV dec^{-1} for CZIF-67, CPt@ZIF-67, carbon

 This journal is © The Royal Society of Chemistry 2019

Open Access Article. Published on 25 February 2019. Downloaded on 2/7/2026 11:01:58 AM.
This article is licensed under a Creative Commons Attribution 3.0 Unported Licence.

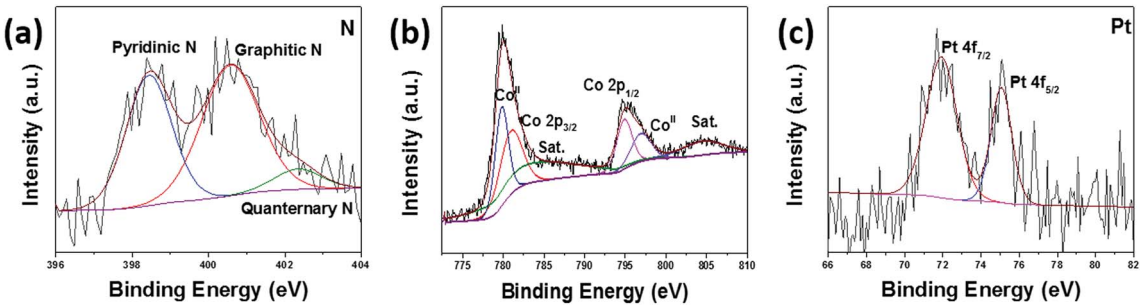

Fig. 2 XPS spectra of (a) nitrogen, (b) cobalt, and (c) platinum in CPt@ZIF-67.

black and 20 wt% Pt/C, respectively (Fig. 3b). The results indicate that the HER follows the Volmer–Heyrovsky mechanism.[44,45] It is worth mentioning that additional tests were carried out on 20 wt% Pt/C (Fig. S12a†); the Tafel slopes calculated from these three new tests were identically 35.5 mV dec^{-1}, which is slightly poorer than previous literature values (31 mV dec^{-1}).[46,47] This data demonstrates the same trend as the polarization curves. CPt@ZIF-67 outperformed the commercial 20 wt% Pt/C. The exceptionally low Tafel slope of 27.1 mV dec^{-1} at a low potential for CPt@ZIF-67 represents nearly 30% improvement over commercial 20 wt% Pt/C. A 24 hour stability test with CPt@ZIF-67 and 20 wt% Pt/C was carried out, as shown in Fig. 3c, where the activity decays are virtually negligible for CPt@ZIF-67 in comparison with 20 wt% Pt/C. This could be attributed to the catalyst being protected by the carbon shell from erosion by the acidic electrolyte. The morphology and structure of the catalyst are well-retained, since Fig. S6b, c, S9c and S10b† show that there is imperceptible change in CPt@ZIF-67 before and after stability tests. Assuming all Pt atoms are active sites to the acidic electrolyte, approximately 4.01 × 10^{16} sites cm^{-2} are accessible to the electrolyte, which is more than in Pt(111) (1.5 × 10^{15} sites cm^{-2}).[48] Then, the turnover frequency (TOF) of the HER was calculated (ESI note 1†). The TOFs of CPt@ZIF-67 are 2.94 and 0.80 s^{-1} at η = 100 and 50 mV, respectively, much better than other published noble-metal or non-noble metal-based catalysts (Table S4†). Likewise, compared with other reported HER catalysts, including Pt alloy (Table 1), the present Tafel slope was a record low for HER electrocatalysts.

The electrochemically active surface area (ECSA) was calculated by measuring the total charge of the H$_{upd}$

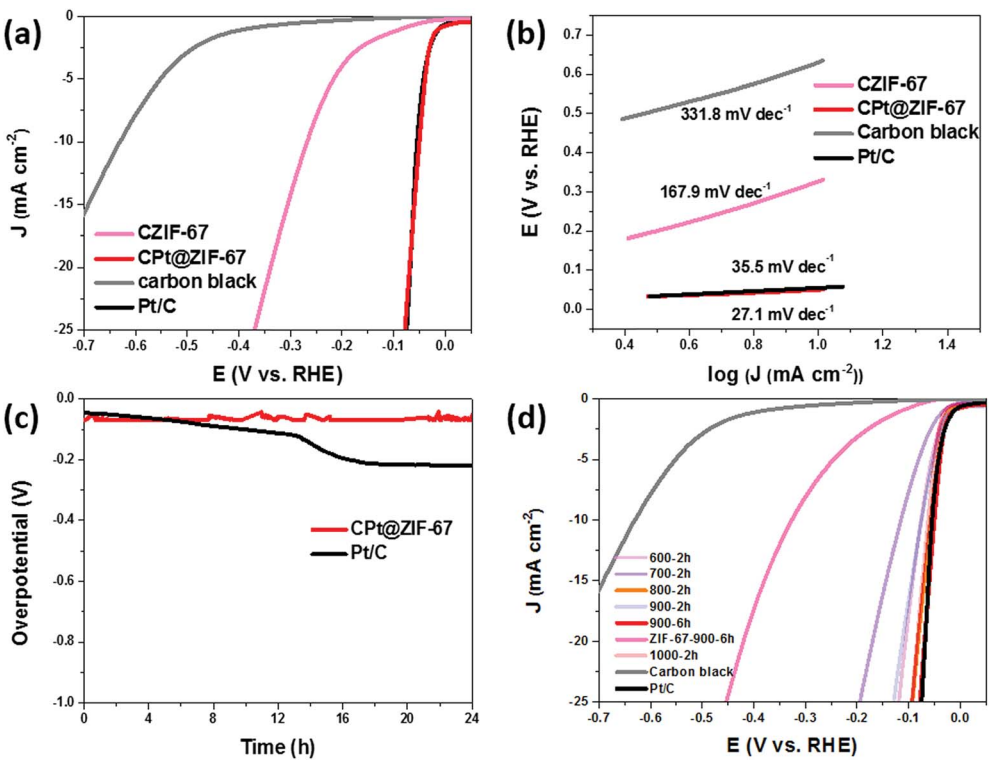

Fig. 3 (a) Polarization curves of CZIF-67, CPt@ZIF-67, carbon black and 20 wt% Pt/C. (b) Tafel plots of CZIF-67, CPt@ZIF-67, carbon black and 20 wt% Pt/C. (c) *I*–*t* curve of CPt@ZIF-67 and 20 wt% Pt/C up to 24 hours. (d) Polarization curves of carbonized Pt-doped ZIF-67 at 600 °C for 2 h, 700 °C for 2 h, 800 °C for 2 h, 900 °C for 2 h, 900 °C for 6 h, 1000 °C for 2 h, carbon black and 20 wt% Pt/C.

Open Access Article. Published on 25 February 2019. Downloaded on 2/7/2026 11:01:58 AM.
This article is licensed under a Creative Commons Attribution 3.0 Unported Licence.

Table 1 Summary of representative HER catalysts in acidic electrolyte

Catalyst	Electrolyte	Overpotential at 10 mA cm^{-2} (mV)	Tafel slope (mV dec^{-1})	Reference
CPt@ZIF-67	0.5 M H_2SO_4	50	27	This work
ALD50Pt/NGNs	0.5 M H_2SO_4	45	29	49
Co@BCN	0.5 M H_2SO_4	96	64	50
NiMo-NGTs	0.5 M H_2SO_4	65	67	51
Co_2P@NPG	0.5 M H_2SO_4	130	58	52
WS_2 nanosheets	0.5 M H_2SO_4	230	60	53
N, P-graphene	0.5 M H_2SO_4	420	91	54
Cu_3P@NPPC-650	0.5 M H_2SO_4	292	76	55
MoS_2/RGO	0.5 M H_2SO_4	140	41	56
Pt-SnS_2	0.5 M H_2SO_4	117	69	57
MoS_2/graphene	0.5 M H_2SO_4	150	41	58
Pt-MoS_2	0.5 M H_2SO_4	—	52	59
Pd ND/DR-MoS_2	0.5 M H_2SO_4	208	66	60
Au-MoS_2	0.5 M H_2SO_4	—	69	61
Ru-C_3N_4	0.5 M H_2SO_4	140	57	62

adsorption/desorption region.[63] The specific ECSA (ECSA per unit weight of metal) of CPt@ZIF-67 is 64.3 $m^2 g^{-1}$ pt (ESI note 2†) is slightly higher than that of commercial 20 wt% Pt/C (63 $m^2 g^{-1}$ pt).[64] To further understand the electrocatalytic activity of CPt@ZIF-67 for HER, we performed electrochemical impedance spectroscopy (EIS). The Nyquist plots of the EIS results are demonstrated in Fig. S13.† The Nyquist plot of CPt@ZIF-67 gave a similar semicircle to that of commercial 20 wt% Pt/C. This result is another proof that CPt@ZIF-67 affords similar kinetics as the commercial catalyst (with only a quarter of the Pt amount).

The mass density comparison is shown in Fig. S14.† At an overpotential of 10 mV, CPt@ZIF-67 exhibited a mass density of 0.87 A mg^{-1} Pt, which is about 4 times higher than that obtained by commercial 20 wt% Pt/C (0.22 A mg^{-1} Pt). This outstanding electrocatalytic activity of CPt@ZIF-67 may be ascribed to the uniformly dispersed PtCo clusters spread over a relatively large surface area for electrochemical reactions, even at a relatively low overall loading (5 wt%). More importantly, a downshift of the Pt D-band may exist for Pt electronic structure when PtCo alloy is formed, due to the charge localization between Co and Pt.[65] This should reduce the desorption energy of protons around the Pt site, facilitating formation of H_2 gas molecules.

The effects of annealing temperature and time on CPt@ZIF-67 for HER performance were also investigated, as shown in Fig. 3d. As expected, the activities are in the following order: CPt@ZIF-67-900-6 > CPt@ZIF-67-800-2 > CPt@ZIF-67-1000-2 > CPt@ZIF-67-900-2 > CPt@ZIF-67-600-2 > CPt@ZIF-67-700-2. The results suggest that both porosity and metal clustering of the catalysts play important roles. Meanwhile, the longer annealing time seems to outperform the short one, possibly by yielding higher crystallinity of carbon to enhance the conductivity of the catalysts.

Density functional theory (DFT) calculations were carried out to further clarify the effects of alloying on the metal cluster embedded nitrogen-doped carbon catalysts. Predominately, $|\Delta G(H^*)|$ is a good descriptor for HER activity and should be close to zero to balance H* adsorption and desorption within the reaction steps.[66] The chosen models included the metal clusters, *e.g.* Co_{55} cluster, and Pt-doped Co clusters with different Pt/Co ratios, as shown in Fig. S15.† The C_{240} fullerene ball was adopted to mimic the outer carbon coating for the metal clusters, as in previous studies.[67,68] Furthermore, to avoid DFT description failure on the open shell d-electrons of the transition metal, DFT+U, originally proposed by Anisimov *et al.*,[69] was adopted to appropriately treat the strongly correlated electron intra-atomic Coulomb (U) and exchange (J) interactions within a HF-like theory, while the rest of the system was treated with pure DFT.

Unlike the simple cubic Co_{55} metal clusters used in previous studies, the model here was adopted from the global minima with the Gupta potential, as shown in Fig. S15a.† The energy difference of those two clusters was 1.05 eV per atom, which is too great to be ignored. Furthermore, Pt doping positions were also considered, including corner, edge and body positions. As shown in Table S5,† for $PtCo_{54}$, a single Pt atom tended to occupy the edge positions (Fig. S15b†). This conclusion is consistent with a recent publication where Pt atoms enrich the edge positions of dodecahedral Pt/Ni clusters.[70] It should also be noted that both doping at the corner and edge positions was exothermic, while replacement at the body position was endothermic. For Pt_2Co_{53} (Fig. S15c†), the formation energy is listed in Table S6.† Dual Pt atoms preferred to dope the edge and body positions (Fig. S15c†). Clearly, only surface doped Pt could act as an effective active site for HER. Bader analysis was also carried out to study electron transfer within the metal alloy cluster.[71] The results show that the average valence electrons on Pt increased by 0.77e and 0.87e for PtC_{54} and Pt_2Co_{53}, respectively. This is also in agreement with the observations in our XPS and PXRD analyses. According to the D-band theory, this charge transfer to the active sites can further reduce the overpotential.

The details of calculation of the HER free energy are provided in the Methods section, and different adsorption/desorption sites of H* were also considered, as shown in Fig. S16.† The calculated free energy diagrams of a single-layer carbon shell

 This journal is © The Royal Society of Chemistry 2019

Open Access Article. Published on 25 February 2019. Downloaded on 2/7/2026 11:01:58 AM.
This article is licensed under a Creative Commons Attribution 3.0 Unported Licence.

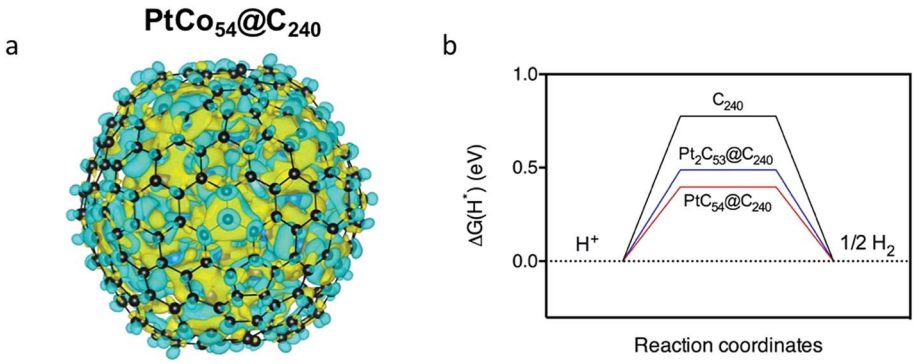

Fig. 4 (a) The electron density difference in $PtCo_{54}@C_{240}$, where blue and yellow represent areas of electron accumulation and diminishing, respectively. (b) The free energy diagram of HER on C_{240}, $PtCo_{54}@C_{240}$ and $Pt_2Co_{53}@C_{240}$.

and a carbon shell within different PtCo alloy clusters are shown in Fig. 4b. Compared with bare C_{240}, the free energy was dramatically reduced, by 48.6%, if the metal cluster was inside the carbon shell. For different levels of Pt doping, the energy barrier of the structure with 2 Pt atoms was 90.1 meV higher than that of single Pt doped. Hence, the "extra" Pt atom in $Pt_2Co_{53}@C_{240}$ does not provide an additional active site or lower the energy barrier for activation. Therefore, catalyst performance did not linearly increase with Pt doping level. The free energy of the metal-only clusters was also calculated for comparison, as seen in Fig. S17.† Though the metal-only clusters possess a lower free energy (0.12 eV), they were difficult to stabilize in the practical environment, due to the lack of a ligand stabilizer. The electron density difference with/without the C-shell, $PtCo_{54}@C_{240}$, was also calculated, shown in Fig. 4a. The electron density seems to accumulate at the outside of the carbon cage, which is in line with the Raman shifts in our experiment section. This charge redistribution could greatly facilitate the attraction/sorption of H^+ for the HER reaction.

Conclusions

PtCo cluster-embedded porous carbon catalysts were effectively synthesized *via* Pt-doped ZIF-67 formation and subsequent tailored carbonization, leading to nitrogen-doped and finely dispersed PtCo clusters firmly anchored over the derived porous carbon. The resulting catalyst (CPt@ZIF-67) exhibits extraordinary performance for HER in 0.5 M H_2SO_4, achieving a Tafel slope of 27.1 mV dec^{-1} with an overpotential of only 50 mV at the reference current density of 10 mA cm^{-2}, which is four times the mass-specific energy density of the commercial counterpart (20 wt% Pt/C), even at a much lower Pt loading of 5 wt%.

The improvement is partly attributed to the ease of charge transfer from the metal cluster to lower the D-band centre, the high electron conductivity of the well-integrated carbon substrate, and the richness of N-functional groups, along with the good dispersion of fine clusters over large surface area. Meanwhile, the catalysts also possessed excellent stability, with negligible loss of activity for up to 24 hours in an acidic electrolyte. DFT calculations revealed that Pt doping in the Co cluster does not always favour the surface sites to impart direct benefit to HER. Hence, additional Pt doping does not proportionally enhance HER activity. The carbon cage outside the metal clusters is more electronegative, which also enhances H^+ sorption for HER. Overall, this approach harnessed several beneficial effects to generate a very effective HER catalyst as a low cost and highly stable alternative to commercial 20 wt% Pt/C for hydrogen production. It also provides a design strategy for low Pt loading over surfaces to impart effectiveness at a lower material cost. The catalyst could also be a strong candidate for an overall water splitting process in the future.

Conflicts of interest

There are no conflicts to declare.

Acknowledgements

The authors acknowledge the used of the UCL Grace High performance computing facility (Grace@UCL), and associated support services, in the completion of the simulation work. The authors would also like to acknowledge the support by EPSRC (Grant no. EP/L0183301/1 and EP/K021192/1) and Keysight Technologies, Inc. J. Guo would like to thank the China Scholarship Council (CSC). UK Catalysis Hub is kindly thanked for resources and support provided *via* our membership of the UK Catalysis Hub Consortium and funded by EPSRC (grants EP/K014706/2, EP/K014668/1, EP/K014854/1, EP/K014714/1 and EP/M013219/1). This research has been performed with the use of facilities at the Research Complex at Harwell including MP-AES equipment. The authors would like to thank the Research Complex for access and support to these facilities and equipment. The details are on the Hub website here: http://www.ukcatalysishub.co.uk/pubs.

References

1 C. Xu, S. Peng, C. Tan, H. Ang, H. Tan, H. Zhang and Q. Yan, *J. Mater. Chem. A*, 2014, **2**, 5597–5601.
2 L. Yuan, C. Han, M. Q. Yang and Y. J. Xu, *Int. Rev. Phys. Chem.*, 2016, **35**, 1–36.

Open Access Article. Published on 25 February 2019. Downloaded on 2/7/2026 11:01:58 AM.
This article is licensed under a Creative Commons Attribution 3.0 Unported Licence.

3 N. T. Suen, S. F. Hung, Q. Quan, N. Zhang, Y. J. Xu and H. M. Chen, *Chem. Soc. Rev.*, 2017, **46**, 337–365.
4 N. Cheng, S. Stambula, D. Wang, M. N. Banis, J. Liu, A. Riese, B. Xiao, R. Li, T. K. Sham, L. M. Liu, G. A. Botton and X. Sun, *Nat. Commun.*, 2016, **7**, 13638.
5 Q. Yang, W. Liu, B. Wang, W. Zhang, X. Zeng, C. Zhang, Y. Qin, X. Sun, T. Wu, J. Liu, F. Huo and J. Lu, *Nat. Commun.*, 2017, **8**, 14429.
6 Y. Zhai, D. Pierre, R. Si, W. Deng, P. Ferrin, A. U. Nilekar, G. Peng, J. A. Herron, D. C. Bell, H. Saltsburg, M. Mavrikakis and M. Flytzani-Stephanopoulos, *Science*, 2010, **329**, 1633–1637.
7 H. Yin, S. Zhao, K. Zhao, A. Muqsit, H. Tang, L. Chang, H. Zhao, Y. Gao and Z. Tang, *Nat. Commun.*, 2015, **6**, 6430.
8 J. Greeley, T. F. Jaramillo, J. Bonde, I. Chorkendorff and J. K. Nørskov, *Nat. Mater.*, 2006, **5**, 909–913.
9 S. Bai, C. Wang, M. Deng, M. Gong, Y. Bai, J. Jiang and Y. Xiong, *Angew. Chem., Int. Ed.*, 2014, **53**, 12120–12124.
10 A. B. Laursen, K. R. Patraju, M. J. Whitaker, M. Retuerto, T. Sarkar, N. Yao, K. V. Ramanujachary, M. Greenblatt and G. C. Dismukes, *Energy Environ. Sci.*, 2015, **8**, 1027–1034.
11 H. Fei, Y. Yang, Z. Peng, G. Ruan, Q. Zhong, L. Li, E. L. G. Samuel and J. M. Tour, *ACS Appl. Mater. Interfaces*, 2015, **7**, 8083–8087.
12 S. Chen, J. Duan, M. Jaroniec and S. Z. Qiao, *Angew. Chem., Int. Ed.*, 2013, **52**, 13567–13570.
13 H. Fei, J. Dong, M. J. Arellano-Jiménez, G. Ye, N. Dong Kim, E. L. G. Samuel, Z. Peng, Z. Zhu, F. Qin, J. Bao, M. J. Yacaman, P. M. Ajayan, D. Chen and J. M. Tour, *Nat. Commun.*, 2015, **6**, 8668.
14 J. Deng, P. Ren, D. Deng and X. Bao, *Angew. Chem., Int. Ed.*, 2015, **54**, 2100–2104.
15 B. Y. Xia, Y. Yan, N. Li, H. Bin Wu, X. W. D. Lou and X. Wang, *Nat. Energy*, 2016, **1**, 1–8.
16 H. Ataee-Esfahani, L. Wang, Y. Nemoto and Y. Yamauchi, *Chem. Mater.*, 2010, **22**, 6310–6318.
17 L. Yu, B. Y. Xia, X. Wang and X. W. Lou, *Adv. Mater.*, 2016, **28**, 92–97.
18 S. Dang, Q. L. Zhu and Q. Xu, *Nat. Rev. Mater.*, 2017, **3**, 1–14.
19 S. Gadipelli, T. Zhao, S. A. Shevlin and Z. Guo, *Energy Environ. Sci.*, 2016, **9**, 1661–1667.
20 G. Kresse and J. Furthmüller, *Comput. Mater. Sci.*, 1996, **6**, 15–50.
21 G. Kresse and J. Furthmüller, *Phys. Rev. B*, 1996, **54**, 11169.
22 J. P. Perdew, K. Burke and M. Ernzerhof, *Phys. Rev. Lett.*, 1996, **77**, 3865.
23 P. E. Blöchl, *Phys. Rev. B*, 1994, **50**, 17953.
24 D. Joubert, *Phys. Rev. B*, 1999, **59**, 1758.
25 S. Dudarev and G. Botton, *Phys. Rev. B*, 1998, **57**, 1505.
26 L. Wang, T. Maxisch and G. Ceder, *Phys. Rev. B*, 2006, **73**, 195107.
27 J. K. Nørskov, T. Bligaard, A. Logadottir, J. R. Kitchin, J. G. Chen, S. Pandelov and U. Stimming, *J. Electrochem. Soc.*, 2005, **152**, J23–J26.
28 K. Miwa and A. Fukumoto, *Phys. Rev. B*, 2002, **65**, 155114.
29 S. Gadipelli and Z. X. Guo, *ChemSusChem*, 2015, **8**, 2123–2132.
30 N. Zhang and Y. J. Xu, *Chem. Mater.*, 2013, **25**, 1979–1988.
31 L. Chong, J. Wen, J. Kubal, F. G. Sen, J. Zou, J. Greeley, M. Chan, H. Barkholtz, W. Ding and D.-J. Liu, *Science*, 2018, **362**, 1376.
32 D. Yu, E. Shamsaei, J. Yao, T. Xu and H. Wang, *Inorg. Chem. Front.*, 2017, **4**, 845–849.
33 M. Zhu, J. B. Jasinski and M. A. Carreon, *J. Mater. Chem.*, 2012, **22**, 7684–7686.
34 K. Zhou, B. Mousavi, Z. Luo, S. Phatanasri, S. Chaemchuen and F. Verpoort, *J. Mater. Chem. A*, 2017, **5**, 952–957.
35 F. Zheng, H. Xia, S. Xu, R. Wang and Y. Zhang, *RSC Adv.*, 2016, **6**, 71767–71772.
36 L. Wang, W. Gao, Z. Liu, Z. Zeng, Y. Liu, M. Giroux, M. Chi, G. Wang, J. Greeley, X. Pan and C. Wang, *ACS Catal.*, 2018, **8**, 35–42.
37 L. J. Garces, B. Hincapie, R. Zerger and S. L. Suib, *J. Phys. Chem. C*, 2015, **119**, 5484–5490.
38 X. Zhang and K. Y. Chan, *J. Mater. Chem.*, 2002, **12**, 1203–1206.
39 Y. Sun, J. Lopez, H. W. Lee, N. Liu, G. Zheng, C. L. Wu, J. Sun, W. Liu, J. W. Chung, Z. Bao and Y. Cui, *Adv. Mater.*, 2016, **28**, 2455–2461.
40 D. Zhou, Y. Cui, P.-W. Xiao, M.-Y. Jiang and B.-H. Han, *Nat. Commun.*, 2014, **5**, 4716.
41 K. Artyushkova, B. Kiefer, B. Halevi, A. Knop-Gericke, R. Schlogl and P. Atanassov, *Chem. Commun.*, 2013, **49**, 2539–2541.
42 J. Chen, Y. Yang, J. Su, P. Jiang, G. Xia and Q. Chen, *ACS Appl. Mater. Interfaces*, 2017, **9**, 3596–3601.
43 A. L. Wang, X. J. He, X. F. Lu, H. Xu, Y. X. Tong and G. R. Li, *Angew. Chem., Int. Ed.*, 2015, **54**, 3669–3673.
44 Y. Zheng, Y. Jiao, Y. Zhu, L. H. Li, Y. Han, Y. Chen, A. Du, M. Jaroniec and S. Z. Qiao, *Nat. Commun.*, 2014, **5**, 3783.
45 M. Zeng and Y. Li, *J. Mater. Chem. A*, 2015, **3**, 14942–14962.
46 J. Su, Y. Yang, G. Xia, J. Chen, P. Jiang and Q. Chen, *Nat. Commun.*, 2017, **8**, 14969.
47 P. Jiang, Y. Yang, R. Shi, G. Xia, J. Chen, J. Su and Q. Chen, *J. Mater. Chem. A*, 2017, **5**, 5475–5485.
48 Y. Xue, B. Huang, Y. Yi, Y. Guo, Z. Zuo, Y. Li, Z. Jia, H. Liu and Y. Li, *Nat. Commun.*, 2018, **9**, 1460.
49 N. Cheng, S. Stambula, D. Wang, M. N. Banis, J. Liu, A. Riese, B. Xiao, R. Li, T. K. Sham, L. M. Liu, G. A. Botton and X. Sun, *Nat. Commun.*, 2016, **7**, 13638.
50 H. Zhang, Z. Ma, J. Duan, H. Liu, G. Liu, T. Wang, K. Chang, M. Li, L. Shi, X. Meng, K. Wu and J. Ye, *ACS Nano*, 2015, **10**, 684–694.
51 T. Wang, Y. Guo, Z. Zhou, X. Chang, J. Zheng and X. Li, *ACS Nano*, 2016, **10**, 10397–10403.
52 M. Zhuang, X. Ou, Y. Dou, L. Zhang, Q. Zhang, R. Wu, Y. Ding, M. Shao and Z. Luo, *Nano Lett.*, 2016, **16**, 4691–4698.
53 D. Voiry, H. Yamaguchi, J. Li, R. Silva, D. C. B. Alves, T. Fujita, M. Chen, T. Asefa, V. B. Shenoy, G. Eda and M. Chhowalla, *Nat. Mater.*, 2013, **12**, 850–855.
54 Y. Zheng, Y. Jiao, L. H. Li, T. Xing, Y. Chen, M. Jaroniec and S. Z. Qiao, *ACS Nano*, 2014, **8**, 5290–5296.
55 R. Wang, X. Y. Dong, J. Du, J. Y. Zhao and S. Q. Zang, *Adv. Mater.*, 2018, **30**, 1–10.

This journal is © The Royal Society of Chemistry 2019

Open Access Article. Published on 25 February 2019. Downloaded on 2/7/2026 11:01:58 AM.
This article is licensed under a Creative Commons Attribution 3.0 Unported Licence.

56 Y. Li, H. Wang, L. Xie, Y. Liang, G. Hong and H. Dai, *J. Am. Chem. Soc.*, 2011, **133**, 7296–7299.
57 G. Liu, Y. Qiu, Z. Wang, J. Zhang, X. Chen, M. Dai, D. Jia, Y. Zhou, Z. Li and P. Hu, *ACS Appl. Mater. Interfaces*, 2017, **9**, 37750–37759.
58 Y. Li, H. Wang, L. Xie, Y. Liang, G. Hong and H. Dai, *J. Am. Chem. Soc.*, 2011, **133**, 7296–7299.
59 W. Ren, H. Zhang and C. Cheng, *Electrochim. Acta*, 2017, **241**, 316–322.
60 K. Qi, S. Yu, Q. Wang, W. Zhang, J. Fan, W. Zheng and X. Cui, *J. Mater. Chem. A*, 2016, **4**, 4025–4031.
61 T. Wang, L. Liu, Z. Zhu, P. Papakonstantinou, J. Hu, H. Liu and M. Li, *Energy Environ. Sci.*, 2013, **6**, 625–633.
62 Y. Peng, B. Lu, L. Chen, N. Wang, J. E. Lu, Y. Ping and S. Chen, *J. Mater. Chem. A*, 2017, **5**, 18261–18269.
63 B. Lim, M. Jiang, P. H. C. Camargo, E. C. Cho, J. Tao, X. Lu, Y. Zhu and Y. Xia, *Science*, 2009, **324**, 1302–1305.
64 P. Wu, H. Lv, T. Peng, D. He and S. Mu, *Sci. Rep.*, 2014, **4**, 1–6.
65 X. Han, F. Cheng, T. Zhang, J. Yang, Y. Hu and J. Chen, *Adv. Mater.*, 2014, **26**, 2047–2051.
66 J. Greeley, T. F. Jaramillo, J. Bonde, I. Chorkendorff and J. K. Nørskov, *Nat. Mater.*, 2006, **5**, 909–913.
67 H. Zhang, Z. Ma, J. Duan, H. Liu, G. Liu, T. Wang, K. Chang, M. Li, L. Shi, X. Meng, K. Wu and J. Ye, *ACS Nano*, 2016, **10**, 684–694.
68 J. Su, Y. Yang, G. Xia, J. Chen, P. Jiang and Q. Chen, *Nat. Commun.*, 2017, **8**, 14969.
69 V. I. Anisimov, J. Zaanen and O. K. Andersen, *Phys. Rev. B*, 1991, **44**, 943.
70 N. Becknell, Y. Son, D. Kim, D. Li, Y. Yu, Z. Niu, T. Lei, B. T. Sneed, K. L. More, N. M. Markovic, V. R. Stamenkovic and P. Yang, *J. Am. Chem. Soc.*, 2017, **139**, 11678–11681.
71 W. Tang, E. Sanville and G. Henkelman, *J. Phys.: Condens. Matter*, 2009, **21**, 84204–84210.